

Influence of tissue absorption and scattering on the depth dependent sensitivity of Raman fiber probes investigated by Monte Carlo simulations

Carina Reble,^{1,2,*} Ingo Gersonde,¹ Chad A. Lieber,³ and Jürgen Helfmann¹

¹*Laser- und Medizin-Technologie Berlin (LMTB), Fabekstraße 60-62, 14195 Berlin, Germany*

²*Institute for Optics and Atomic Physics, Technical University Berlin, 10587 Berlin, Germany*

³*CHOC Research Institute, Children's Hospital of Orange County, 455 South Main Street, Orange, California 92868, USA*

*c.reble@lmtb.de

Abstract: We present a Monte Carlo model, which we use to calculate the depth dependent sensitivity or sampling volume of different single fiber and multi-fiber Raman probes. A two-layer skin model is employed to investigate the dependency of the sampling volume on the absorption and reduced scattering coefficients in the near infrared wavelength range (NIR). The shape of the sampling volume is mainly determined by the scattering coefficient and the wavelength dependency of absorption and scattering has only a small effect on the sampling volume of a typical fingerprint spectrum. An increase in the sampling depth in nonmelanoma skin cancer, compared to normal skin, is obtained.

©2011 Optical Society of America

OCIS codes: (170.3660) Light propagation in tissue; (170.5660) Raman spectroscopy; (120.4570) Optical design of instruments; (170.3890) Medical optical instrumentation

References

1. A. S. Haka, K. E. Shafer-Peltier, M. Fitzmaurice, J. Crowe, R. R. Dasari, and M. S. Feld, "Diagnosing breast cancer by using Raman spectroscopy," *Proc. Natl. Acad. Sci. U.S.A.* **102**(35), 12371–12376 (2005).
2. N. Stone, and P. Matousek, "Advanced transmission Raman spectroscopy: a promising tool for breast disease diagnosis," *Cancer Res.* **68**(11), 4424–4430 (2008).
3. M. D. Keller, E. M. Kanter, C. A. Lieber, S. K. Majumder, J. Hutchings, D. L. Ellis, R. B. Beaven, N. Stone, and A. Mahadevan-Jansen, "Detecting temporal and spatial effects of epithelial cancers with Raman spectroscopy," *Dis. Markers* **25**(6), 323–337 (2008).
4. C. A. Lieber, S. K. Majumder, D. L. Ellis, D. D. Billheimer, and A. Mahadevan-Jansen, "In vivo nonmelanoma skin cancer diagnosis using Raman microspectroscopy," *Lasers Surg. Med.* **40**(7), 461–467 (2008).
5. A. Nijssen, K. Maquelin, L. F. Santos, P. J. Caspers, T. C. Bakker Schut, J. C. den Hollander, M. H. Neumann, and G. J. Puppels, "Discriminating basal cell carcinoma from perilesional skin using high wave-number Raman spectroscopy," *J. Biomed. Opt.* **12**(3), 034004 (2007).
6. J. Mo, W. Zheng, J. J. H. Low, J. Ng, A. Ilancheran, and Z. Huang, "High wavenumber Raman spectroscopy for in vivo detection of cervical dysplasia," *Anal. Chem.* **81**(21), 8908–8915 (2009).
7. E. M. Kanter, E. Vargis, S. Majumder, M. D. Keller, E. Woeste, G. G. Rao, and A. Mahadevan-Jansen, "Application of Raman spectroscopy for cervical dysplasia diagnosis," *J Biophotonics* **2**(1-2), 81–90 (2009).
8. M. G. Shim, B. C. Wilson, E. Marple, and M. Wach, "Study of Fiber-Optic Probes for in Vivo Medical Raman Spectroscopy," *Appl. Spectrosc.* **53**(6), 619–627 (1999).
9. N. D. Magee, J. S. Villaumie, E. T. Marple, M. Ennis, J. S. Elborn, and J. J. McGarvey, "Ex vivo diagnosis of lung cancer using a Raman miniprobe," *J. Phys. Chem. B* **113**(23), 8137–8141 (2009).
10. R. O. P. Draga, M. C. M. Grimbergen, P. L. M. Vijverberg, C. F. P. van Swol, T. G. N. Jonges, J. A. Kummer, and J. L. H. Ruud Bosch, "In vivo bladder cancer diagnosis by high-volume Raman spectroscopy," *Anal. Chem.* **82**(14), 5993–5999 (2010).
11. J. T. Motz, M. Hunter, L. H. Galindo, J. A. Gardecki, J. R. Kramer, R. R. Dasari, and M. S. Feld, "Optical fiber probe for biomedical Raman spectroscopy," *Appl. Opt.* **43**(3), 542–554 (2004).
12. Z. Huang, S. K. Teh, W. Zheng, J. Mo, K. Lin, X. Shao, K. Y. Ho, M. Teh, and K. G. Yeoh, "Integrated Raman spectroscopy and trimodal wide-field imaging techniques for real-time in vivo tissue Raman measurements at endoscopy," *Opt. Lett.* **34**(6), 758–760 (2009).
13. J. Mo, W. Zheng, and Z. Huang, "Fiber-optic Raman probe couples ball lens for depth-selected Raman measurements of epithelial tissue," *Biomed. Opt. Express* **1**(1), 17–30 (2010).

14. P. Matousek, I. P. Clark, E. R. C. Draper, M. D. Morris, A. E. Goodship, N. Everall, M. Towrie, W. F. Finney, and A. W. Parker, "Subsurface probing in diffusely scattering media using spatially offset Raman spectroscopy," *Appl. Spectrosc.* **59**(4), 393–400 (2005).
15. N. Stone, R. Baker, K. Rogers, A. W. Parker, and P. Matousek, "Subsurface probing of calcifications with spatially offset Raman spectroscopy (SORS): future possibilities for the diagnosis of breast cancer," *Analyst (Lond.)* **132**(9), 899–905 (2007).
16. M. D. Keller, S. K. Majumder, and A. Mahadevan-Jansen, "Spatially offset Raman spectroscopy of layered soft tissues," *Opt. Lett.* **34**(7), 926–928 (2009).
17. P. Matousek, and N. Stone, "Emerging concepts in deep Raman spectroscopy of biological tissue," *Analyst (Lond.)* **134**(6), 1058–1066 (2009).
18. J. R. Maher, and A. J. Berger, "Determination of ideal offset for spatially offset Raman spectroscopy," *Appl. Spectrosc.* **64**(1), 61–65 (2010).
19. J. C. Day, R. Bennett, B. Smith, C. Kendall, J. Hutchings, G. M. Meaden, C. Born, S. Yu, and N. Stone, "A miniature confocal Raman probe for endoscopic use," *Phys. Med. Biol.* **54**(23), 7077–7087 (2009).
20. T. Katagiri, Y. S. Yamamoto, Y. Ozaki, Y. Matsuura, and H. Sato, "High axial resolution Raman probe made of a single hollow optical fiber," *Appl. Spectrosc.* **63**(1), 103–107 (2009).
21. T. J. Pfefer, K. T. Schomacker, M. N. Ediger, and N. S. Nishioka, "Multiple-fiber probe design for fluorescence spectroscopy in tissue," *Appl. Opt.* **41**(22), 4712–4721 (2002).
22. C. Zhu, Q. Liu, and N. Ramanujam, "Effect of fiber optic probe geometry on depth-resolved fluorescence measurements from epithelial tissues: a Monte Carlo simulation," *J. Biomed. Opt.* **8**(2), 237–247 (2003).
23. A. M. K. Enejder, T.-W. Koo, J. Oh, M. Hunter, S. Sasic, M. S. Feld, and G. L. Horowitz, "Blood analysis by Raman spectroscopy," *Opt. Lett.* **27**(22), 2004–2006 (2002).
24. P. Matousek, M. D. Morris, N. Everall, I. P. Clark, M. Towrie, E. Draper, A. Goodship, and A. W. Parker, "Numerical simulations of subsurface probing in diffusely scattering media using spatially offset Raman spectroscopy," *Appl. Spectrosc.* **59**(12), 1485–1492 (2005).
25. W. C. Shih, K. L. Bechtel, and M. S. Feld, "Intrinsic Raman spectroscopy for quantitative biological spectroscopy part I: theory and simulations," *Opt. Express* **16**(17), 12726–12736 (2008).
26. N. Everall, P. Matousek, N. MacLeod, K. L. Ronayne, and I. P. Clark, "Temporal and spatial resolution in transmission Raman spectroscopy," *Appl. Spectrosc.* **64**(1), 52–60 (2010).
27. M. D. Keller, R. H. Wilson, M.-A. Mycek, and A. Mahadevan-Jansen, "Monte Carlo model of spatially offset Raman spectroscopy for breast tumor margin analysis," *Appl. Spectrosc.* **64**(6), 607–614 (2010).
28. A. Ishimaru, "Wave Propagation and Scattering in Random Media," IEEE Press, Oxford University Press: Oxford 1997.
29. C. Reble, I. Gersonde, S. Andree, H. J. Eichler, and J. Helfmann, "Quantitative Raman spectroscopy in turbid media," *J. Biomed. Opt.* **15**(3), 037016 (2010).
30. A. N. Bashkatov, E. A. Genina, V. I. Kochubey, and V. V. Tuchin, "Optical properties of human skin, subcutaneous and mucous tissues in the wavelength range from 400 to 2000nm," *J. Phys. D Appl. Phys.* **38**(15), 2543–2555 (2005).
31. R. M. Doornbos, R. Lang, M. C. Aalders, F. W. Cross, and H. J. C. M. Sterenberg, "The determination of *in vivo* human tissue optical properties and absolute chromophore concentrations using spatially resolved steady-state diffuse reflectance spectroscopy," *Phys. Med. Biol.* **44**(4), 967–981 (1999).
32. S.-H. Tseng, A. Grant, and A. J. Durkin, "In vivo determination of skin near-infrared optical properties using diffuse optical spectroscopy," *J. Biomed. Opt.* **13**(1), 014016 (2008).
33. G. Zonios, and A. Dimou, "Light scattering spectroscopy of human skin *in vivo*," *Opt. Express* **17**(3), 1256–1267 (2009).
34. S.-H. Tseng, P. Bargo, A. Durkin, and N. Kollias, "Chromophore concentrations, absorption and scattering properties of human skin *in-vivo*," *Opt. Express* **17**(17), 14599–14617 (2009).
35. S. Jacques, <http://omlc.ogi.edu/news/jan98/skinoptics.html>, last accessed 15.5.2010.
36. E. Salomatina, B. Jiang, J. Novak, and A. N. Yaroslavsky, "Optical properties of normal and cancerous human skin in the visible and near-infrared spectral range," *J. Biomed. Opt.* **11**(6), 064026 (2006).
37. H. Ding, J. Q. Lu, W. A. Wooden, P. J. Kragel, and X. H. Hu, "Refractive indices of human skin tissues at eight wavelengths and estimated dispersion relations between 300 and 1600 nm," *Phys. Med. Biol.* **51**(6), 1479–1489 (2006).
38. I. Barman, G. P. Singh, R. R. Dasari, and M. S. Feld, "Turbidity-corrected Raman spectroscopy for blood analyte detection," *Anal. Chem.* **81**(11), 4233–4240 (2009).
39. R. Steponavičius, and S. N. Thennadil, "Extraction of chemical information of suspensions using radiative transfer theory to remove multiple scattering effects: application to a model two-component system," *Anal. Chem.* **81**(18), 7713–7723 (2009).

1. Introduction

Raman spectroscopy is a powerful analytical tool due to its ability to provide molecular information without the need for exogenous labels. Applications of this technique in biomedical research are rapidly increasing, including the diagnosis of breast [1,2], skin [3–5] and cervical cancer [6,7], among others. In order to use Raman spectroscopy as a tool for real-time medical diagnostics, the spectra from a suspicious lesion need to be obtained in clinically

feasible measurement times (few seconds and less) while using low laser powers. This motivates the use of measurement geometries that optimize the light throughput of the detection system, which is typically limited by the spectrograph, leading to measurement volumes larger than achievable by confocal Raman microscopy. For many *in vivo* applications, Raman fiber probes provide the required flexibility to access the tissue sites. Most Raman fiber probes are so called high-volume probes, which interrogate a relatively large tissue volume ($\approx 1 \text{ mm}^3$). While single fiber measurements with a $200 \text{ }\mu\text{m}$ fiber have been reported in the high wavenumber region [5], many fingerprint Raman probes consist of a central illumination fiber surrounded by several detection fibers with integrated filters [8–13]. Some probes increase the overlap of excitation and detection area by beam-steering [8] or use lenses on the distal end of the probe to efficiently collect the backscattered light [10,13], while others utilize adjacent excitation and detection spots [9]. Another approach is to increase the spatial offsets of excitation and detection spots (spatially offset Raman spectroscopy, SORS) to enhance the fraction of subsurface signal [14–18]. To improve the signal contribution of a specific thin tissue layer, *e.g.* for the detection of epithelial cancer, confocal probes [19,20] can be employed to reduce the signal contribution from other tissue layers.

This variety of probe geometries leads to respective differences in the portion(s) of tissue interrogated by each probe. Thus, when selecting the most suitable Raman probe for a specific application, it is important to predict the tissue volume which contributes to the signal, often called measurement volume, interrogation volume or sampling volume, to accurately ascribe sources of the collected Raman signal. In addition to the measurement geometry, the sampling volume depends on the absorption and scattering properties of the sample itself. Therefore, accurate biochemical interpretation of Raman measurements requires accounting for both the optical geometry of the Raman probe as well as the tissue architecture-specific optical properties, to assess respective Raman signal contributions from various tissue strata.

Here we use the Monte Carlo (MC) method to calculate the spatial distribution of Raman sensitivity depending on the measurement geometry and the optical properties of the sample. Similar calculations have been performed previously for fluorescence measurements [21,22]. MC models for Raman scattering have been previously developed by Enejder et al. [23] for predicting the effect of measurement geometry on the detected Raman signal of blood. A MC model for SORS measurements of layered turbid media was developed by Matousek et al. [24]. Shih et al. used a MC model to validate their method to correct Raman spectra for the influence of scattering and absorption [25]. The MC calculation of spatial resolution and sensitivity with focus on non-absorbing samples was shown by Everall et al. [26]. Recently, Keller et al. adapted a fluorescence code for the prediction of SORS measurements [27], where the sensitivity for detected Raman photons originating from a certain depth was calculated. Further, Mo et al. [13] developed a MC code to simulate the sampling volume of a ball-lens fiber probe depending on diameter and refractive index of the ball lens and probe-tissue distance. However, previous simulations of sampling volumes use fixed optical parameters and the influence of absorption and scattering on the sampling volume has not yet been investigated systematically.

In this study, we applied our MC method to calculate the sampling volume of a 0.2 mm and 2 mm single fiber probe as well as a SORS configuration and a widely used 7-around-1 multi fiber probe [9,10]. We show how the sampling volume of these probes varies depending on the absorption coefficient μ_a and the reduced scattering coefficient μ_s' typical for skin in the near infrared wavelength range (NIR), the results of which can be generalized to other epithelial tissues. For the 7-around-1 probe, the sampling volume variation over the fingerprint range (785-910 nm) for a typical skin spectrum was investigated. Further, we compared the sampling volume in nonmelanoma skin cancer to the sampling volume in normal skin and investigated the effect on the sampling volume if μ_a and μ_s' of both skin layers vary independently in the range of the literature values. Finally, we investigated the influence of the probe-tissue interface on the sampling volume.

2. Materials and methods

2.1 Model for Raman scattering in turbid media and determination of spatial distribution of sensitivity

Here we give a detailed motivation for our Monte Carlo method. As the number of Raman processes is very small compared to elastic scattering and absorption, we have not introduced an explicit Raman process in our method as this would be statistically inefficient.

In this article, we use the following definitions:

- Position vector: r , unit vector defining propagation direction: s
- Radiance: $L(r,s)$ in units of photons/(s mm² sr)
- Phase function for elastic scattering: $p(s,s')$
- Total radiance: $\Phi(r) = \int_{\Omega} L(r,s) d\Omega$ in units of photons/(s mm²)
- Detector signal: S corresponding to an excitation power of 1 photon / s
- Raman-scattering coefficient: $\mu_{Raman}(r) = \sigma_{Raman} c_{Raman}(r)$ in units of mm⁻¹
- Scattering coefficient: μ_s in units of mm⁻¹
- Reduced scattering coefficient: $\mu_s' = \mu_s (1-g)$ with $g = 0.8$ in units of mm⁻¹
- Total attenuation coefficient: $\mu_t = \mu_a + \mu_s$ in units of mm⁻¹
- Raman-scattering cross section: σ_{Raman} in units of mm²
- Number density of the Raman active molecule: c_{Raman} in units of mm⁻³

With $\mu_{Raman} \ll \mu_a$, μ_s' we neglect multiple Raman scattering of photons. In this case we can define a radiance $L^{Exc}(r,s)$ which describes the light distribution of excitation at wavelength λ_{Exc} and a radiance $L^{Raman}(r,s)$ for Raman scattered light with the Stokes shifted wavelength. Both quantities are given by the well known radiative transport equation [28] with optical parameters corresponding to the excitation or Stokes shifted wavelength:

$$\frac{dL(r,s)}{ds} = -\mu_t(r)L(r,s) + \mu_s(r) \int_{\bar{\Omega}} p(s,\bar{s})L(r,\bar{s})d\bar{\Omega} + Q(r,s) \quad (1)$$

$$\int_{\bar{\Omega}} p(s,\bar{s})d\bar{\Omega} = \int_{\Omega} p(s,\bar{s})d\Omega = 1$$

Here $p(s,s')$ is the phase function for elastic scattering and Q is a volume source term. Further, s and \bar{s} denote directions of propagation and Ω is a solid angle. For the excitation radiance $Q(r,s) = 0$ in most cases, as the illumination of the probe is taken into account by boundary conditions of the radiation transport equation. Under the assumption of single Raman scattering, it can be shown that the source term for the Raman scattered radiance is

$$Q^{Raman}(r,s) = \mu_{Raman}(r) \int_{\Omega} p_{Raman}(s,\bar{s})L^{exc}(r,\bar{s})d\Omega = \frac{\mu_{Raman}(r)}{4\pi} \Phi^{exc}(r) \quad (2)$$

The right hand side in the above equation follows by assuming that Raman scattering is isotropic. Integrating Q^{Raman} over all directions, we get the number density n_{Raman} of Raman scattering processes:

$$\int_{\Omega} Q^{Raman}(r,s)d\Omega = \mu_{Raman}(r)\Phi^{exc}(r) = n_{Raman}(r) \quad (3)$$

Here we used the second line of Eq. (1), so the approximation in Eq. (2) is not necessary.

As there are no boundary sources for L^{Raman} it follows from Eq. (1) that L^{Raman} is a linear function of Q^{Raman} and can therefore be written using a Green's function:

$$L^{\text{Raman}}(r, s) = \iint_{\bar{r}, \bar{\Omega}} G(r, s, \bar{r}, \bar{s}) Q^{\text{Raman}}(\bar{r}, \bar{s}) d\bar{\Omega} d^3\bar{r} \quad (4)$$

$G(r, s, \bar{r}, \bar{s})$ is the radiance resulting from a point source at \bar{r}' radiating in direction \bar{s}' . Any Raman detector signal S_{Raman} is a linear functional of L^{Raman} . It follows from Eqs. (2), (3) and (4) with the assumption that Raman scattering is isotropic that the Raman signal can be written as

$$S_{\text{Raman}} = \int_r f(r) \Phi^{\text{exc}}(r) \mu_{\text{Raman}}(r) d^3r = \int_r f(r) n_{\text{Raman}}(r) d^3r \quad (5)$$

In Eq. (5), $f(r)$ is the detected Raman signal for an isotropic point source of radiation located at r with the Stokes shifted wavelength.

We define a function $w(r)$ which can be considered as the spatial sensitivity distribution of the measurement, which is the quantity of interest here:

$$w(r) := f(r) \Phi^{\text{exc}}(r) \Rightarrow S_{\text{Raman}} = \int_r w(r) \mu_{\text{Raman}}(r) d^3r$$

In the following, the range of r values where $w(r)$ is large is considered as the sampling volume of the Raman measurement.

The total radiance is related to the number density of absorption or scattering processes and the corresponding coefficients for excitation radiation:

$$\Phi^{\text{exc}}(r) = \frac{n_{\text{Raman}}(r)}{\mu_{\text{Raman}}(r)} = \frac{n_{\text{abs}}^{\text{exc}}(r)}{\mu_a(r)} = \frac{n_{\text{scatter}}^{\text{exc}}(r)}{\mu_s(r)}$$

Thus, in the Monte Carlo method Φ^{exc} can be represented by an ensemble of absorption or scattering processes with number density $n_{\text{abs}}^{\text{exc}}(r)$ or $n_{\text{scatter}}^{\text{exc}}(r)$ gained from an ensemble of excitation photons. With Eq. (5) we have

$$S_{\text{Raman}} = \int_r f(r) \frac{\mu_{\text{Raman}}(r)}{\mu_a(r)} n_{\text{abs}}^{\text{exc}}(r) d^3r = \int_r f(r) \frac{\mu_{\text{Raman}}(r)}{\mu_s(r)} n_{\text{scatt}}^{\text{exc}}(r) d^3r \quad (6)$$

$$w(r) = f(r) \frac{n_{\text{abs}}^{\text{exc}}(r)}{\mu_a(r)} = f(r) \frac{n_{\text{scatt}}^{\text{exc}}(r)}{\mu_s(r)}$$

In our Monte Carlo method, $f(r)$ is calculated with an ensemble of photon trajectories with N_{photon} members starting at position r with an isotropic distribution of initial directions and counting the number of photons which reach the detector:

$$f(r) = \lim_{N_{\text{photon}} \rightarrow \infty} \frac{1}{N_{\text{photon}}} \sum_{i=1}^{N_{\text{photon}}} d_i; \quad d_i = \begin{cases} 1 & \text{if photon hits detector} \\ 0 & \text{else} \end{cases}$$

Correspondingly, S_{Raman} is calculated in the following way: calculating the trajectories of N_{photon} excitation photons results in an ensemble of N_{abs} absorption positions r_{abs} of excitation photons. Each position is used as the starting position for a Raman scattered photon. Again the number of photons which reach the detector are counted. As the quantity r_{abs} is a random variable with probability density $n_{\text{abs}}^{\text{exc}}(r)$ one can show that S_{Raman} in Eq. (6) is given by

$$S_{\text{Raman}} = \int_r f(r) \frac{\mu_{\text{Raman}}(r)}{\mu_a(r)} n_{\text{abs}}^{\text{exc}}(r) d^3r = \lim_{N_{\text{photon}} \rightarrow \infty} \frac{1}{N_{\text{photon}}} \sum_{i=1}^{N_{\text{abs}}} d_i \frac{\mu_{\text{Raman}}(r_{\text{abs},i})}{\mu_a(r_{\text{abs},i})}.$$

Here the factor $1/N_{\text{photon}}$ is due to the normalization of S_{Raman} to an excitation power of one photon per second.

For $\mu_s > \mu_a$, it is statistically more efficient to use the elastic scattering processes to represent Φ^{exc} .

For a stratified medium where all quantities depend on the depth coordinate z only we define a depth sensitivity function $w_z(z)$ which is the integral of $w(r)$ over lateral coordinates leading to

$$S_{\text{Raman}} = \int_z w_z(z) \mu_{\text{Raman}}(z) dz. \quad (7)$$

For a homogeneous medium it follows that

- $\int w(z) dz$ is the Raman signal S_{Raman} normalized by the molecule specific μ_{Raman} , previously named $\text{Ram}_T / \mu_{\text{Raman}}$ in units of mm [29].
- $\Delta z w(z) / \int w(z) dz$ is the fraction of the detected Raman signal originating from a z -interval with thickness Δz .

With the exception of the results in Fig. 2a below, we neglect the Stokes shift of the Raman photon energy for the sake of simplicity.

2.2. Fiber probe geometries

Single fiber measurements were simulated by defining an overlapping excitation and detection spot of identical diameter d with $d = 0.2$ mm or $d = 2$ mm as well as intermediate and smaller diameters. The illumination and acceptance angle was set according to the fiber numerical aperture (NA) of 0.22. These models of measurements geometries apply also to non-contact measurements, where the images of excitation and detection fibers coincide on the sample surface.

For the SORS probe, a spatial offset $r = 0.4$ mm was set between an excitation and detection fiber with $d = 0.2$ mm and $\text{NA} = 0.22$. The 7-around-1 probe consists of a central excitation fiber with 400 μm diameter surrounded by 7 detection fibers with 300 μm diameter, each with $\text{NA} = 0.22$ as per [8]. The distance between the centers of source and detection fibers was set to 385 μm , which accounts for the thicknesses of the respective claddings. The filters on the distal end of the probe were neglected and we assumed a closed silica shield to be in contact with the skin. For all probe geometries the refractive index n of the probe was set to 1.45. For comparison with an air-skin interface, n was set to 1.

2.3. Skin model

As a skin model, we used a two-layer geometry consisting of an epidermis with a thickness of 100 μm and a semi-infinite dermis. The optical properties of skin in the wavelength range of 785–910 nm were chosen based on the literature, which we briefly review here in order to give an impression of the large range of reported values. Many reported values of μ_a and μ_s' were obtained by *in vivo* diffuse reflectance measurements and therefore correspond to a weighted average of epidermal and dermal optical properties [31–34], while only a few characterized both layers separately [35,36]. The wavelength dependent change of optical properties is comparable or lower than the sample-to-sample variation and the variation among different references. According to the model of Jacques [35], which is based on measurements of rat skin, the absorption coefficient of the epidermis μ_{a_epi} ranges from 0.15 mm^{-1} to 0.91 mm^{-1} at 785 nm and from 0.09 mm^{-1} to 0.58 mm^{-1} at 910 nm, depending on the melanosome concentration. The values of Salomatina et al. range from 0.19 \pm 0.07 mm^{-1} at 785 nm to 0.08 \pm 0.04 mm^{-1} at 910 nm [36], where the error is the sample-to-sample variation.

The absorption coefficient of the dermis, μ_{a_derm} , according to Jacques ranges from 0.025 mm^{-1} to 0.049 mm^{-1} (with negligible wavelength dependency) for blood volume fractions of

0-5% while the values of Salomatina range from $0.15 \pm 0.03 \text{ mm}^{-1}$ at 785 nm to $0.08 \pm 0.02 \text{ mm}^{-1}$ at 910 nm. The scattering of epidermis and dermis is considered to be similar by Jacques ($\mu_s' = 1.8 \text{ mm}^{-1}$ at 785 nm to 1.2 at 910 nm) while Salomatina et al. report $3.6 \pm 0.3 \text{ mm}^{-1}$ at 785 nm and $3.2 \pm 0.3 \text{ mm}^{-1}$ at 910 nm for the epidermis and $2.2 \pm 0.2 \text{ mm}^{-1}$ at 785 nm and $2.0 \pm 0.2 \text{ mm}^{-1}$ at 910 nm for the dermis. Literature values with mixed contributions of both layers range from $\mu_a = 0.01 \text{ mm}^{-1}$ [31] to 0.25 mm^{-1} [30] (and references therein) and $\mu_s' = 0.6 \text{ mm}^{-1}$ [31] to 5 mm^{-1} [36]. The refractive index of skin was selected as 1.43 ± 0.1 for the epidermis (including stratum corneum) and 1.38 ± 0.2 for the dermis in the wavelength range of interest, as measured by Ding et al. [37]. The g factor, which describes the anisotropy of the Henyey-Greenstein phase function for elastic scattering, was set to 0.8 for both layers as this is a typical value for tissue.

3. Results and discussion

3.1. Influence of absorption and scattering on sampling volume of different fiber probe geometries

In order to focus on the geometry dependent effects in this section, we used here a skin model with matched absorption and scattering coefficients of epidermis and dermis using parameters as typically reported for *in vivo* diffuse reflectance measurements in the NIR, see section 2.3. The normalized depth dependent sensitivity $w_z(z) / \int w_z(z) dz$ or sampling volume of four different fiber probe geometries is shown in Fig. 1a-d.

As expected from previous simulations for fluorescence probes and Raman measurement geometries [21,24,27], the sampling depth increases with fiber diameter and spatial offset. Further, we show here that in the investigated parameter range, the shape of the sampling volume depends mainly on μ_s' , independent of the specific fiber probe geometry. For the single fiber measurement with $d = 0.2 \text{ mm}$, variations of μ_a by one order of magnitude have only a negligible effect on the shape of the sampling volume, see Fig. 1a. In contrast, a ten times increase in μ_s' shifts the sensitivity towards shallower depths. For the single fiber measurement with $d = 2 \text{ mm}$, a ten times increase of μ_a shifts the sensitivity towards shallower depths, but in a lower magnitude as the effect of a ten times increase in μ_s' , see Fig. 1b. In the SORS geometry, with the same fiber diameters as in the first case but a spatial offset of 0.4 mm, a ten times increase in μ_a also shifts the sensitivity towards shallower depths, see Fig. 1c. The effect of a ten times increase in μ_s' is again larger as it is demonstrated by a large shift of the sensitivity maximum. Interestingly, in this configuration the depth of maximal sensitivity seems to depend only on μ_s' . In the case of the 7-around-1 fiber probe, the results are similar as for the SORS probe, which might be due to the fact that the chosen spatial offset is similar to the center-to-center distance of excitation and detection fibers in the 7-around-1 probe, see Fig. 1d.

In Fig. 1e, we show how the total radiance Φ^{exc} of excitation photons depends on z for the same parameters as used for Fig. 1d. It can be seen that the slope of the depth dependent decrease is much smaller than for the normalized sensitivity. The corresponding $w_z(z)$ is presented in Fig. 1f. Integration of $w_z(z)$ over z leads to the detected Raman signal intensity $S_{\text{Raman}}/\mu_{\text{Raman}}$ as defined by Eq. (7). As previously described for the detected Raman signal intensity, $w_z(z)$ increases with decreasing μ_a as well with increasing μ_s' [25,29]. Further analysis of the influence of scattering and absorption on the intensity of the detected Raman signal is not within the scope of this article.

To detect changes in the Raman signal of the dermal layers it is useful to reduce the signal contribution of tissue below the dermis, because this will enhance the signal contrast between different states of the dermal layers. Moreover, variations in the contribution of deeper tissue may affect the analysis of the measurement adversely (e.g. chemometric analysis). The same argument holds if changes in the Raman signal of the epidermis are to be analyzed.

The total fraction of Raman signal originating from a certain tissue depth can be obtained by integrating the normalized $w_z(z)$ over the z range of interest. In our 2-layer tissue model,

the dermis is semi-infinite, with $z > 0.1$ mm. For a quantitative comparison of the different fiber probe geometries we compared the signal fractions originating from depths $z < 0.1$ mm (epidermis), $z < 0.7$ mm or $z < 1$ mm, see Table 1. We chose the optical parameters $\mu_a = 0.01$ mm⁻¹ and $\mu_s' = 1$ mm⁻¹, which are rather low values for skin, and therefore the resulting sampling depth is an upper limit for skin. In addition to the fiber probe geometries used above, sensitivity distributions have been calculated for single fibers with $d = 0.4$ mm, $d = 0.1$ mm, $d = 0.05$ mm and $d = 0.01$ mm. It is obvious that a fiber diameter $d = 0.2$ mm is required

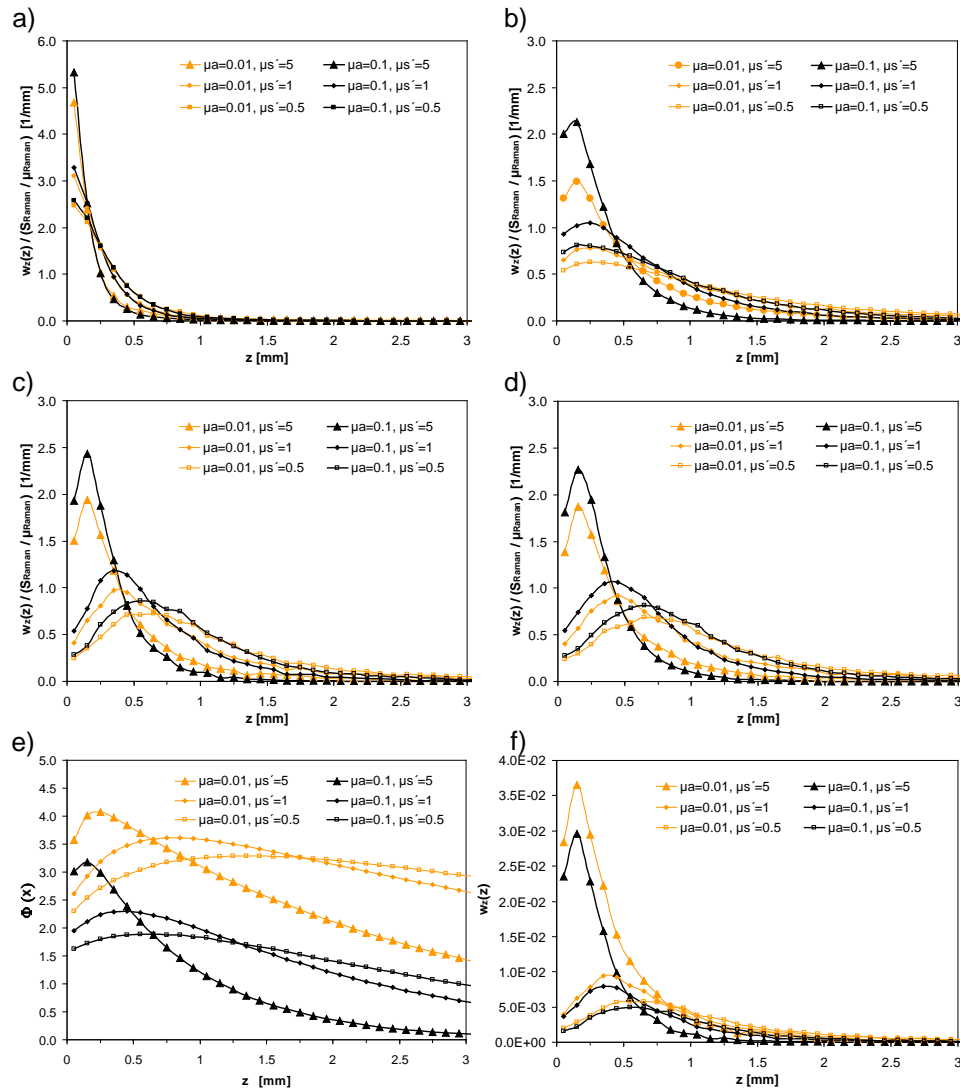


Fig. 1. Dependency of $w_s(z) / \int w_s(z) dz$ on μ_a and μ_s' in mm⁻¹ for a) single fiber measurement with $d = 0.2$ mm b) single fiber measurement with $d = 2$ mm c) SORS measurement with $d = 0.2$ mm and $r = 0.4$ mm d) 7-around-1 probe with $d_{ex} = 0.4$ mm, $d_{det} = 0.3$ mm and $r = 0.385$ mm e) Dependency of Φ^{exc} on μ_a and μ_s' in mm⁻¹ for 7-around-1 probe e) Dependency of $w_s(z)$ on μ_a and μ_s' in mm⁻¹ for 7-around-1 probe. Error bars are not shown to maintain clarity, but deviation from a smooth curve shape is due to statistical errors.

to ensure that contributions of tissue at $z > 1$ mm are below 5%. Aiming at measuring $\approx 95\%$ of the signal from the $100\mu\text{m}$ thick epithelium requires even $d < 0.01\text{mm}$ (at $\text{NA} = 0.22$).

Choosing an optimal probe design based on these results is however not trivial. It depends on whether the analysis is limited by non systematic variance of the spectra, which is mainly due to the variance of normal surrounding tissue, or rather limited by detector noise. In the latter case, it is preferable to maximize the systematic signal of interest and admit higher contributions of deeper tissue, which is achievable by larger fiber diameters and/or higher NA of the probe. Increasing the NA was found to cause a slight shift of the sampling volume towards lower z values (data not shown).

In order to link the values in Table 1 directly to measurement data, one has to keep in mind that we have assumed a homogeneous Raman scatterer distribution and normalized the data with respect to μ_{Raman} . For inhomogeneous Raman scatterer distributions the integral in Eq. (7) must be calculated. But if a homogeneously distributed bioconstituent produces a distinct Raman peak, then the signal fractions in Table 1 can be directly interpreted as fraction of the Raman peak size.

Table 1. Signal contribution from $z < 0.1$ mm, $z < 0.7$ mm and $z < 1.0$ mm for the 7-around-1 fiber probe, the SORS geometry and single fibers with different diameters

$\mu_a = 0.01 \text{ mm}^{-1}$, $\mu_s' = 1 \text{ mm}^{-1}$	7-around-1	$d = 0.2 \text{ mm}$, $r = 0.4 \text{ mm}$	$d = 2 \text{ mm}$	$d = 0.4 \text{ mm}$	$d = 0.2 \text{ mm}$	$d = 0.1 \text{ mm}$	$d = 0.05 \text{ mm}$	$d = 0.01 \text{ mm}$
Signal from $z < 0.1 \text{ mm}$	4%	4%	7%	20%	31%	45%	61%	93%
Signal from $z < 0.7 \text{ mm}$	54%	51%	55%	86%	94%	97%	99%	100%
Signal from $z < 1.0 \text{ mm}$	70%	68%	64%	90%	96%	98%	99%	100%

3.2. Influence of skin optical properties on sampling volume of a typical 7-around-1 Raman fiber probe

Using the 7-around-1 probe geometry as an example, we investigated the wavelength dependent variation of the sampling volume that can occur when a typical fingerprint spectrum (785 nm-910 nm) is measured. The wavelength dependency of absorption and scattering plays a role since each Raman band in the spectrum is determined by the propagation of the photons according to the optical parameters at the excitation wavelength (μ_{a_ex} , $\mu_{s'_ex}$), and after the Raman scattering, by the propagation according to the optical parameters at the Stokes shifted wavelength (μ_{a_st} , $\mu_{s'_st}$).

The effect on the sampling volume is shown in Fig. 2a, where we compared the case of zero Stokes shift to the case where the Raman photon propagates with optical properties corresponding to a maximal Stokes shift of $\approx 1800 \text{ cm}^{-1}$ at 910 nm, using the optical parameters measured by Salomatina et al. [36]. The resulting difference in sampling volume, which is an upper limit for the sampling volume variation over the whole NIR skin spectrum, is fairly small. The corresponding signal fractions originating from $z < 0.7$ mm (1.0 mm) are 81% (91) % for the zero Stokes shift case and 84% (93) % for the maximal Stokes shift case, see Table 2. We further define the 70% (90%)-sampling depth as the depth where 70% (90%) signal contribution is obtained from the tissue above. For the 70% (90%)-sampling depth we obtain 0.43 mm (0.90 mm) for the zero Stokes shift case and 0.46 mm (0.83 mm) for the maximal Stokes shift case. Thus, this dispersion effect on the sampling volume seems negligible for the chosen spectral range and tissue type. Consequently, individual Raman bands in a NIR skin spectrum originate from a similar sampling volume. However, the effect may be stronger in the visible or mid-infrared spectral range.

In the same graph, we show that comparable results can be obtained for the sampling volume using the mean optical properties of excitation and Stokes shifted wavelength in the simulation while neglecting the Stokes shift.

Next, we investigated how diagnostically relevant changes of μ_a and μ_s' can affect the sampling volume. In the spectral range of interest here, Salomatina et al. [36] reported a

decrease of both μ_s' and μ_a for nodular basal cell carcinoma (BCC) and squamous cell carcinoma (SCC) compared to normal tissue. Since the thickness of the cancerous tissue samples in [35] were between 0.17 and 0.85 mm, we set the optical properties of both epidermis and dermis to the values reported for nodular BCC and SCC, respectively. In Fig. 2b we show that the variation in optical properties found in the cancerous tissue shifts the sampling volume to higher z values, corresponding to signal contributions for $z < 1.0$ mm of 80% (82%) for nodular BCC (SCC) versus 93% in case of normal skin, see Table 2. For the 70% (90%)-sampling depth we obtained 0.44 mm (0.84 mm) for the normal tissue, 0.70 mm (1.34 mm) for the nodular BCC and 0.70 mm (1.44 mm) for SCC. However, these results are not valid for early stages of skin cancer, which typically originates in the epidermis, because we assumed that the cancer tissue is semi-infinite.

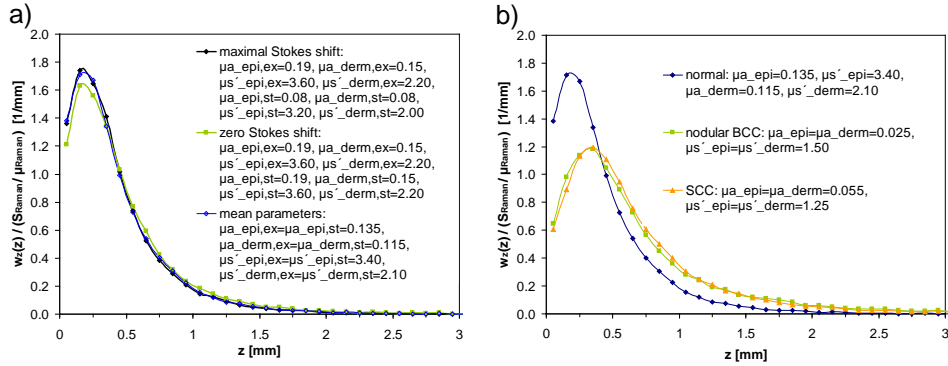


Fig. 2. Dependency of $w_z(z) / \int w_z(z) dz$ on optical properties of skin (in mm^{-1}) for the 7-around-1 fiber probe. a) Optical properties corresponding to the case of maximal Stokes shift and zero Stokes shift are used. In addition, the maximal Stokes shift case is compared to the case when mean optical parameters of excitation and maximal Stokes shift photons are used. b) Optical properties of normal skin, nodular basal cell carcinoma (BCC) as well as squamous cell carcinoma (SCC) are used.

Table 2. Signal contribution from $z < 0.1$ mm, $z < 0.7$ mm and $z < 1.0$ mm for the 7-around 1 fiber probe for the optical properties specified in Fig. 2

	Zero Stokes shift	Max. Stokes shift	Mean/normal	Nodular BCC	SCC
Signal from $z < 0.1$ mm	12%	14%	14%	6%	6%
Signal from $z < 0.7$ mm	81%	84%	84%	66%	66%
Signal from $z < 1.0$ mm	91%	93%	93%	80%	82%

Finally, we investigated the variation of the sampling volume when the optical parameters of each skin layer are varied independently. We chose the parameters such that the complete range of literature values described in section 2.3 was covered, only $\mu_s' < 1 \text{ mm}^{-1}$ was omitted for clarity and because we found only one reference that reported such low values.

As in section 3.1, the μ_s' determines the depth of the sensitivity peak while large variations of μ_a cause only moderate changes in the shape of the sampling volume.

In Fig. 3a, the μ_s' of both layers is matched while the μ_a varied independently. The influence of μ_a on the normalized sensitivity is very small, which indicates a minor influence of skin pigmentation on the sampling volume.

The influence of μ_s' is however larger, as demonstrated per Fig. 3b, where μ_s' is varied and μ_a of both layers is matched. An increase of μ_s' from 1 to 5 mm^{-1} even leads to the same depth of maximal sensitivity as for a $\mu_s' = 5 \text{ mm}^{-1}$ in both layers, but the overall sensitivity distribution is still significantly different compared to the case of matched μ_s' . This indicates that variations of μ_s' of external or natural origin are a major source of sampling volume variation. The signal contributions originating from certain tissues regions for some representative data of Fig. 3 are given in Table 3.

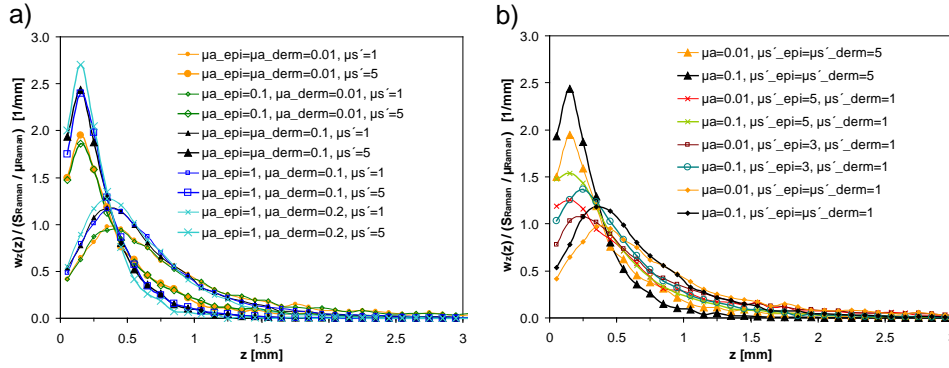


Fig. 3. Dependency of $w_r(z)/\int w_r(z)dz$ on typical optical properties of skin for the 7-around-1 fiber probe. a) μ_{a_epi} and μ_{a_derm} (in mm^{-1}) are varied independently. b) $\mu_{s'_epi}$ is varied independently

Table 3. Signal contribution from $z < 0.1$ mm, $z < 0.7$ mm and $z < 1.0$ mm for the 7-around 1 fiber probe for representative parameter combinations of the data in Fig. 4

μ_{a_epi} [mm^{-1}], $\mu_{s'_epi}$ [mm^{-1}]	0.01, 1	0.01, 5	0.1, 1	0.1, 3	0.1, 5	0.1, 5	1.0, 1	1.0, 5	1.0, 1	1.0, 5
μ_{a_derm} [mm^{-1}], $\mu_{s'_derm}$ [mm^{-1}]	0.01, 1	0.01, 5	0.1, 1	0.1, 1	0.1, 1	0.1, 5	0.1, 1	0.1, 5	0.2, 1	0.2, 5
signal from $z < 0.1$ mm	4%	15%	5%	10%	15%	19%	5%	17%	6%	20%
signal from $z < 0.7$ mm	54%	81%	65%	74%	78%	92%	65%	92%	70%	95%
signal from $z < 1.0$ mm	70%	90%	82%	86%	88%	97%	82%	97%	86%	99%

3.3. Influence of tissue-probe interface on sampling volume

In order to investigate the influence of the probe-skin interface, we compared calculations for a silica-skin interface and an air-skin interface for the 7-around-1 probe, a situation which could be obtained by imaging the fiber probe onto the tissue surface or by an air-gap between probe and tissue. Figure 4 shows the results for different μ_a and $\mu_{s'}$, which are matched for both layers. The normalized sensitivity is similar for high z values but shifts towards superficial tissue in the range of lower z values. This means that if the coupling of the probe to the skin is interrupted by an air gap, the normalized sensitivity changes mainly in a depth z below ≈ 1 mm. This can be explained by the fact that total reflection at the skin-air interface reduces the photon escape probability and thus leads to longer average pathlengths through the Raman scattering medium. In case of the silica-skin interface, there is no total reflection since the refractive index of silica is slightly higher than the refractive index of the epidermis. This influence of the probe-tissue interface was negligible for the $d = 0.2$ mm single fiber geometry (data not shown).

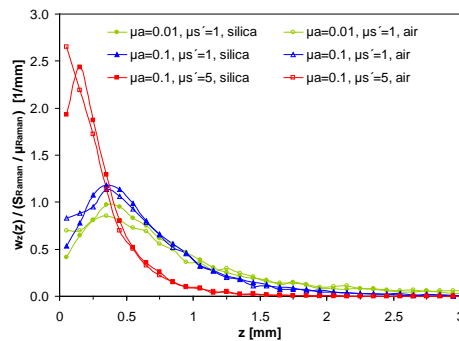


Fig. 4. Dependency of $w_s(z)/\int w_s(z)dz$ on the refractive index of the medium which is in contact with the skin for the 7-around-1 probe. The μ_a and μ_s' (in mm^{-1}) of both layers is matched.

4. Conclusion

The depth dependent sensitivity of a given measurement geometry is of fundamental importance for the interpretation of Raman spectral measurements.

Our results show that independent of the investigated fiber probe geometry, an increase in tissue scattering as well as an increase in absorption shifts the sampling volume to shallower depths. However, in the investigated range of optical parameters and probe geometries, differences in tissue absorption have a smaller influence on the shape of the sampling volume than variations in scattering.

As Raman spectroscopy is increasingly applied for the discrimination of cancerous versus normal tissue, the change of optical properties in cancerous tissue should be accounted for in the interpretation of the Raman measurement. In the case of the 7-around-1 probe geometry, our results show that the variation of optical properties increases the 70% (90%)-sampling depth by 0.26 mm (0.50 mm) or 0.26 mm (0.60 mm), when nodular BCC or SCC is compared to normal skin. This previously unaccounted disparity in sampling volume may inherently cause variations in the respective tissue spectra, potentially creating artifactual band assignments in the correlation of spectra with pathologic biochemistry. In order to accurately link the MC results to real measurement values of a layered tissue, the distribution of Raman scatterers as well as potentially different Raman cross sections of constituents contributing to the same band need to be taken into account.

For a typical NIR fingerprint spectrum of skin, the dispersion of absorption and scattering has only a small effect on the sampling volume, which means that individual Raman bands in a spectrum originate from a similar sampling volume. However, the effect may be larger in the visible or mid-infrared spectral range as well as for other tissues.

In addition to the variations in depth dependent sensitivity or sampling volume, it must be kept in mind that variations in absorption and scattering also change the intensity of the detected Raman signal. Even in a homogeneous system, where sampling volume variations are not relevant, the intensity of the Raman band is modulated by variations of absorption and scattering. This is important if Raman band intensities of different samples are compared quantitatively or if ratios of Raman bands at different wavelengths are analyzed. In case of the examples shown in Fig. 2, the Raman band intensity at maximum Stokes shift relative to the intensity at zero Stokes shift is 93% and the mean Raman intensity of BCC (SCC) relative to the intensity of normal tissue is 114% (92%). Further analysis of the effect of varying scattering and absorption on the detected Raman signal intensity and possible correction methods are described elsewhere [25,29,38,39].

For Raman spectral diagnosis of diseased versus normal tissue, identifying and/or isolating contributions from epithelial layers may provide increased discriminant abilities.

Assuming that the analysis of the subtle spectral changes accompanying precancerous tissue (including chemometric techniques) is limited by the non systematic variance of the

spectra, which is mainly due to the variance of normal surrounding tissue, minimization of signal contributions from surrounding tissue is important. For the detection of epithelial cancer, our results suggest that single fiber geometries of unpractically small diameters would be required to minimize dermal contributions. As single fiber Raman measurements are only suited for high wavenumber measurements, more sophisticated probe designs have been suggested for that purpose [13,19,20].

If the analysis of the Raman measurement is not limited by unsystematic contributions but by detector noise, it will be better to maximize the systematic signal of interest and admit higher contributions of deeper tissue. In this case the optimal probe design might shift to larger fiber diameters and/or higher NA of the probe, depending on instrumental parameters such as available spectrometer étendue and excitation power.

In the future, it might be useful to compare the performances of such confocal and other probe designs in terms of sampling volume and detection efficiency.

Using MC simulations to investigate the sampling volumes of specific probe or measurement geometries can both improve the interpretation of the collected Raman signals as well as guide the design of probes with increased discriminant ability for biomedical diagnostics.

Acknowledgments

The project was co-funded by the Senate of Berlin and the EU (EFRE, FKZ 10138595).